Measuring the Chern number of Hofstadter bands with ultracold bosonic atoms

M. Aidelsburger[1,2], M. Lohse[1,2], C. Schweizer[1,2], M. Atala[1,2], J. T. Barreiro[1,2,3],
S. Nascimbène[4], N. R. Cooper[5], I. Bloch[1,2] & N. Goldman[4,6]

[1] *Fakultät für Physik, Ludwig-Maximilians-Universität, Schellingstrasse 4, 80799 München, Germany*
[2] *Max-Planck-Institut für Quantenoptik,
Hans-Kopfermann-Strasse 1, 85748 Garching, Germany*
[3] *Present address: Department of Physics, University of California, San Diego, California 92093, USA*
[4] *Collège de France, 11 place Marcelin Berthelot &
Laboratoire Kastler Brossel, CNRS, UPMC, ENS, 24 rue Lhomond, 75005 Paris, France*
[5] *T. C. M. Group, Cavendish Laboratory, J.J. Thomson Avenue, Cambridge CB3 0HE, United Kingdom*
[6] *Center for Nonlinear Phenomena and Complex Systems, Université Libre de Bruxelles (U.L.B.), B-1050 Brussels, Belgium*
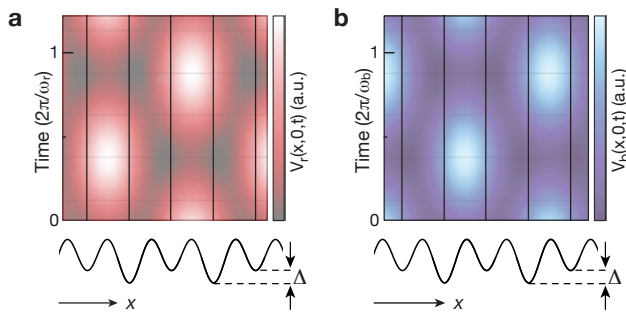
S.I. FLUX RECTIFICATION IN A STAGGERED OPTICAL POTENTIAL

FIG. S1. Total time-dependent potential $V_r(x,0,t)$ **(a)** and $V_b(x,0,t)$ **(b)** as a function of time for $y = 0$. For each of the two modulations (red and blue) the relative modulation amplitude between neighboring sites vanishes on every other bond. The modulation depicted in (a) therefore induces tunneling only on bonds with a positive energy offset $+\Delta$ between neighboring sites and the one depicted in (b) on bonds with negative energy offset $-\Delta$.

In this section we describe the laser configuration used to rectify the artificial magnetic field in a two-dimensional super-lattice potential as illustrated in Fig. 1a of the main text. The staggered energy offset Δ introduced by the staggered super-lattice potential inhibits tunneling along x for $\Delta \gg J_x$, with J_x being the bare tunnel coupling. In our previous work [S1] we used one pair of far-detuned running-wave beams to restore the tunneling along this direction, which results in a staggered effective magnetic field whose sign is alternating along x. In order to rectify this artificially generated magnetic field we now employ two pairs of beams (red and blue arrows in Fig. 1a of the main text), where each of them addresses only every other bond (Fig. S1), such that the sign of the Peierls phases on the two different kinds of bonds (red and blue dashed lines in Fig. 1a of the main text) can be controlled individually. Each pair consists of two beams, along the x- and y-direction, where the ones along x are retro-reflected creating a standing-wave that interferes with the running-wave along y. The correspond-ing local time-dependent optical potential is given by

$$V_i(x,y,t) = 4E_{i1}^2\cos^2(k_L x + \varphi_i) + E_{i2}^2$$
$$+ 4E_{i1}E_{i2}\cos(k_L x + \varphi_i) \times$$
$$\cos(-k_L y + \omega_i t + \phi_i) , \qquad (S.1)$$

where φ_i is the phase relative to the underlying lattice and ϕ_i is the phase of the modulation, $i = \{r,b\}$. The local potential consists of two parts, a static standing-wave term with constant offset and a time-dependent interference term. In Fig. S1 we show the total time-dependent potential V_i for $y = 0$, $\varphi_r = -\pi/4$ and $\varphi_b = \pi/4$. It illustrates that for an appropriate choice of φ_i the relative modulation between neighboring sites vanishes on every other bond. Furthermore if $\varphi_b = \varphi_r + \pi/2$ the two pairs of beams address two different kinds of bonds with positive and negative sign of the energy offset $\pm\Delta$ between neighboring sites. This has the additional advantage that the two standing wave-terms in $V_r(x,y,t)$ and $V_b(x,y,t)$ cancel each other.

In our experimental setup all four beams are realized using a single laser. The beam is split into two parts (beam 1 & 2). Subsequently each of them is sent through a fiber-coupled intensity modulator, which is used to create two sidebands (red and blue) with frequencies $\omega_{rj,bj}$, $j = \{1,2\}$. The carrier frequency is fully suppressed. The frequency differences between each pair of sidebands are given by $\omega_{r1} - \omega_{b1} = 2\pi \times 185\,\text{MHz}$ and $\omega_{r2} - \omega_{b2} = 2\pi \times 185\,\text{MHz} + \Delta/\hbar$. Due to the large frequency difference between the sidebands $\omega_{rj,bj}$ we can neglect the corresponding interference terms, such that the only relevant time-dependent terms for the modulation are given by the interference between ω_{i1} and ω_{i2}. Since the sidebands are generated symmetrically around the carrier frequency, they also have the same amplitudes $E_{rj} = E_{bj} \equiv E_j$. This beam configuration thus leads to a local time-dependent optical potential of the form

$$V_{m,n}(t) = \kappa \cos(m\pi/2 - \pi/4) \times \qquad (S.2)$$
$$\cos(-n\pi/2 + \omega_r t + \phi_r)$$
$$+ \kappa \cos(m\pi/2 + \pi/4) \times$$
$$\cos(-n\pi/2 + \omega_b t + \phi_b) ,$$

with $\kappa = 4E_1 E_2$ and $\omega_i = \omega_{i2} - \omega_{i1}$. The position in the lattice is defined as $\mathbf{R} = m a\hat{\mathbf{e}}_x + n a\hat{\mathbf{e}}_y$, with m,n integers

and $\hat{\mathbf{e}}_{x,y}$ the unit vectors. The relative phase between the two modulations $\phi_b - \phi_r$ can be controlled in the experiment but its value neither influences the value of the effective flux realized by the modulation nor the strength of the effective couplings that appear in the effective Hamiltonian. Therefore, without loss of generality we choose this phase equal to $\phi_b - \phi_r = \pi/2$. The overall phase of the modulation relative to the underlying lattice however is random because the phase of the running-wave along y is not stabilized with respect to the lattice potential and is denoted as ϕ_0, so that the time-dependent potential reads

$$
\begin{aligned}
V_{m,n}(t) = \;& \kappa \, \cos(m\pi/2 - \pi/4) \times && \text{(S.3)}\\
& \cos(-n\pi/2 + \omega_r t + \phi_0)\\
& + \kappa \, \cos(m\pi/2 + \pi/4) \times\\
& \cos(-n\pi/2 + \omega_b t + \pi/2 + \phi_0) \, .
\end{aligned}
$$

For resonant modulation $\omega_r = -\omega_b = \Delta/\hbar$, the total time-dependent Hamiltonian can be mapped onto an effective time-independent Hamiltonian with effective tunneling amplitudes $J_x^{\text{eff}} \simeq J_x \kappa/(\sqrt{2}\Delta)$ and $J_y^{\text{eff}} \simeq J_y$ (see also Sect. S.III). The effective coupling along x is complex with spatially-dependent phases $\phi_{m,n} = \phi_0 + \frac{\pi}{2}(m+n)$, which defines our experimental gauge and results in a flux of $\Phi = \phi_{m,n+1} - \phi_{m,n} = \pi/2$ per plaquette, aligned along the $-\hat{\mathbf{e}}_z$−direction. Note that in the main text and Sect. S.IV of the Supplementary Information we have chosen to describe our system using the Landau gauge $\phi_{m,n} = n\pi/2$ for the sake of simplicity.

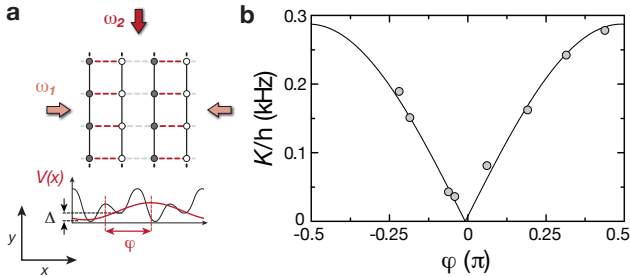## S.II.   LASER-ASSISTED TUNNELING ON EVERY OTHER BOND

FIG. S2.   Suppression of tunneling on every other bond **(a)** Schematic drawing of the experimental setup. Along x a tilted double-well potential with energy offset Δ is used to inhibit tunneling. A pair of beams (red arrows) with frequency difference ω is then used to restore resonant tunneling. The corresponding local optical potential $V(x)$ is shown in red for $y = t = 0$. The relative phase between the modulation and the underlying lattice is denoted as φ **(b)**. The gray data points show the measured effective coupling strength induced by the modulation as a function of the relative phase φ. The solid line is a fit of eq. (S.4), where the amplitude and the phase offset are used as free fit parameters.

Experimentally we studied the applicability of our flux-rectification method by measuring the suppression of tunneling on every other bond using only one pair of the beams mentioned above (see Sect. S.I). The measurement was performed

in isolated tilted double-well potentials (see Fig. S2a), where tunneling on every other bond was suppressed due to a high potential barrier and tunneling within the double well was inhibited due to a potential offset between neighboring sites. We then restored resonant tunneling within the double-wells using only one pair of beams for the modulation and measured the effective tunneling amplitude as a function of φ, the phase relative to the underlying lattice. The effective tunnel coupling is proportional to the relative modulation amplitude between neighboring sites, which can be expressed as

$$
V_{m+1,n}(t) - V_{m,n}(t) = \sqrt{2}\kappa|\sin(\varphi)|\cos(-n\pi/2 + \omega t) \quad \text{(S.4)}
$$

where we have chosen the convention that for $\varphi = 0$ the modulation along x is in phase with the long lattice used to create the double-well potential and thus corresponds to a modulation that is in-phase on the two sites of the double-well and therefore cannot induce tunneling.

The experimental sequence started by loading a Bose-Einstein condensate of ^{87}Rb atoms into a 3D optical lattice of depths $V_z = 30(1) \, \text{Er}_z$, $V_y = 30(1) \, \text{Er}_s$ and $V_{xL} = 35(1) \, \text{Er}_L$, with $\text{Er}_\alpha = \hbar^2 k_\alpha^2/(2m)$, $\alpha = \{s, L, z\}$, and $k_z = 2\pi/\lambda_z$, with $\lambda_z = 844 \, \text{nm}$, $\lambda_s = 767 \, \text{nm}$ and $\lambda_L = 2\lambda_s$. After applying a filtering sequence where all double occupancies were removed, the short lattice along x was ramped up to $V_x = 7.0(2) \, \text{Er}_s$ within 20 ms. The phase of the superlattice was chosen such that a tilted double well with an energy offset of $\Delta/\hbar \approx 4.5 \, \text{kHz}$ was created where all atoms were located in the lower energy sites. Then we switched on the modulation instantaneously in order to induce resonant tunneling. The effective tunnel coupling was then determined by looking at the Rabi oscillations between the left and right wells of the double-well potentials as a function of the holdtime. The corresponding data is shown in Fig. S2. From this we obtain an upper limit for the suppression of tunneling on every second bond of $J_{x,\text{min}}^{\text{eff}}/J_{x,\text{max}}^{\text{eff}} < 0.13$. A residual coupling is most likely due to imperfect reflection of the retro-reflected beam along x.

S.III.   THE EFFECTIVE HARPER-HOFSTADTER HAMILTONIAN

The experimental setup used to rectify the artificial magnetic flux in a two-dimensional superlattice potential as described in Sect. S.I gives rise to an explicitly time-dependent Hamiltonian, which can be separated as

$$
\hat{H}(t) = \hat{H}_0 + \hat{V}(t), \quad \text{(S.5)}
$$

where $\hat{H}_0$ describes the static components, and $\hat{V}(t)$ is the time-dependent modulation.

Considering a single-band tight-binding approximation, the static Hamiltonian $\hat{H}_0$ is taken in the form

$$
\begin{aligned}
\hat{H}_0 = \;& \hat{T}_x + \hat{T}_y + \hat{V}_{\text{conf}} + \hat{U}_{\text{int}} && \text{(S.6)}\\
& + \frac{\Delta}{2}\sum_{m,n}(-1)^m \hat{n}_{m,n} + \frac{\delta}{2}\sum_{m,n}\left[(-1)^m + (-1)^n\right]\hat{n}_{m,n}.
\end{aligned}
$$

The first line includes the confining potential, the nearest-

neighbor hopping and interaction terms,

$$\hat{T}_x = -J_x \sum_{m,n} \hat{a}^\dagger_{m+1,n} \hat{a}_{m,n} + \hat{a}^\dagger_{m-1,n} \hat{a}_{m,n},$$

$$\hat{T}_y = -J_y \sum_{m,n} \hat{a}^\dagger_{m,n+1} \hat{a}_{m,n} + \hat{a}^\dagger_{m,n-1} \hat{a}_{m,n},$$

$$\hat{V}_{\text{conf}} = \sum_{m,n} \hat{n}_{m,n} V_{\text{conf}}(m,n),$$

$$\hat{U}_{\text{int}} = (U/2) \sum_{m,n} \hat{n}_{m,n} (\hat{n}_{m,n} - 1),$$

where $J_{x,y}$ denote the hopping matrix elements, $\hat{a}^\dagger_{m,n}$ creates a particle at lattice site $\boldsymbol{x} = (ma, na)$, a is the lattice spacing, (m,n) are integers and U denotes the on-site interaction strength. The number operator is defined as $\hat{n}_{m,n} = \hat{a}^\dagger_{m,n} \hat{a}_{m,n}$, and the external harmonic trapping potential $V_{\text{conf}}(m,n) \propto (m^2 + n^2)$. The second line in eq. (S.6) describes the main staggered potential with energy offset $\Delta + \delta$ between neighboring sites, which inhibits tunneling along the x direction and an auxiliary weak staggered potential with offset δ along y. The additional offset δ gives rise to a symmetric staggered detuning along both directions, with $\delta \ll \Delta$.

In the tight-binding limit in which we work, the main effect of the additional pairs of beams (see Sect. S.I) is a modulation of the on-site energies, giving a time-dependent contribution to the Hamiltonian of the form

$$\hat{V}(t) = \kappa \sum_{m,n} \hat{n}_{m,n} \{f_r(m) \cos[\omega t + g_r(n)] + f_b(m) \cos[\omega t + g_b(n)]\},$$

$$f_r(m) = \cos(m\pi/2 - \pi/4), \quad f_b(m) = \cos(m\pi/2 + \pi/4),$$

$$g_r(n) = \phi_0 - n\pi/2, \quad g_b(n) = n\pi/2 - \phi_0 - \pi/2, \quad \text{(S.7)}$$

where ϕ_0 is determined by the relative phase between the running-waves along y and the underlying lattice potential, which is not controlled in the current experimental setup (see Sect. S.I). In order to restore the tunneling along the x direction, we fix the modulation frequency ω so as to satisfy the resonance condition $\hbar\omega = \Delta$.

The time-evolution of the system is ruled by the Schrödinger equation $i\hbar\partial_t \psi = \hat{H}(t)\psi$. Let us consider the unitary transformation

$$\psi = \hat{R}(t)\tilde{\psi} = \exp\left(-i\frac{\omega}{2}\hat{W}t\right)\tilde{\psi}, \quad \text{(S.8)}$$

$$\hat{W} = \sum_{m,n} (-1)^m \hat{n}_{m,n}.$$

The transformed state satisfies the Schrödinger equation $i\hbar\partial_t \tilde{\psi} = \tilde{H}(t)\tilde{\psi}$, with the modified Hamiltonian

$$\tilde{H}(t) = \tilde{H}_0 + \hat{V}^{(+1)} e^{i\omega t} + \hat{V}^{(-1)} e^{-i\omega t}, \quad \text{(S.9)}$$

where

$$\tilde{H}_0 = \hat{T}_y + \hat{V}_{\text{conf}} + \hat{U}_{\text{int}} + \frac{\delta}{2} \sum_{m,n} [(-1)^m + (-1)^n] \hat{n}_{m,n} \quad \text{(S.10)}$$

$$\hat{V}^{(+1)} = \frac{\kappa}{2} \sum_{m,n} \hat{n}_{m,n} \, \mathfrak{g}(m,n) - J_x \sum_{m \, \text{odd}, n} \hat{a}^\dagger_{m+1,n} \hat{a}_{m,n} + \hat{a}^\dagger_{m-1} \hat{a}_{m,n},$$

$$\hat{V}^{(-1)} = \frac{\kappa}{2} \sum_{m,n} \hat{n}_{m,n} \, \mathfrak{g}^*(m,n) - J_x \sum_{m \, \text{even}, n} \hat{a}^\dagger_{m+1,n} \hat{a}_{m,n} + \hat{a}^\dagger_{m-1} \hat{a}_{m,n},$$

where

$$\mathfrak{g}(m,n) = f_r(m) e^{i g_r(n)} + f_b(m) e^{i g_b(n)}. \quad \text{(S.11)}$$

We describe the time-evolution of the system by partitioning the evolution operator as

$$\hat{U}(t) = e^{-i\hat{K}(t)} e^{-it\hat{H}_{\text{eff}}/\hbar} e^{i\hat{K}(0)}, \quad \text{(S.12)}$$

where the effective Hamiltonian $\hat{H}_{\text{eff}}$ describes the long-time dynamics, and where the operator $\hat{K}(t)$ captures the micromotion, see Refs. [S2, S3]. Note that the initial kick $e^{i\hat{K}(0)}$, which depends on the initial phase of the modulation, is inhibited in the experiment by launching the modulation adiabatically. Following Ref. [S2], we find that the effective Hamiltonian associated with the general single-harmonic time-dependent Hamiltonian in eq. (S.9) is given by

$$\hat{H}_{\text{eff}} = \tilde{H}_0 + \frac{1}{\hbar\omega}[\hat{V}^{(+1)}, \hat{V}^{(-1)}] \quad \text{(S.13)}$$

$$+ \frac{1}{2(\hbar\omega)^2} \left([[\hat{V}^{(+1)}, \tilde{H}_0], \hat{V}^{(-1)}] + [[\hat{V}^{(-1)}, \tilde{H}_0], \hat{V}^{(+1)}] \right)$$

$$+ \mathcal{O}(1/\omega^3),$$

where we considered a perturbative expansion in powers of $(1/\omega)$. To be explicit, we introduce a small dimensionless quantity $\Omega_{\text{eff}}/\omega \ll 1$, where Ω_{eff} is a typical frequency associated with the effective Hamiltonian (see below). In the following, we will identify Ω_{eff} with the cyclotron frequency associated with the Harper-Hofstadter Hamiltonian (S.17), $\Omega_{\text{eff}} = B/m^*$, where $B = \Phi\hbar/a^2$ is the effective magnetic field, Φ is the related flux per plaquette and $m^* = \hbar^2/(2Ja^2)$ is the effective mass with $J = J_x^{\text{eff}} = J_y$. In the present experimental scheme, the flux will be found to be $\Phi = 2\pi(1/4)$, see eq. (S.17) below, so that we obtain $\Omega_{\text{eff}} = \pi J/\hbar$; hence, the driving should satisfy the high-frequency condition $\hbar\omega = \Delta \gg J$, which is indeed the case in the experiment.

We now evaluate the effective Hamiltonian in eq. (S.13), up to second-order in $(1/\omega)$,

$$\hat{H}_{\text{eff}} = \hat{H}_{\text{eff}}^{(0)} + \hat{H}_{\text{eff}}^{(1)} + \hat{H}_{\text{eff}}^{(2)} + \mathcal{O}(1/\omega^3) \quad \text{(S.14)}$$

using the specific operators defined in eq. (S.10).

The zeroth-order terms

The zeroth order contribution to the effective Hamiltonian is given by the static terms

$$\hat{H}_{\text{eff}}^{(0)} = \tilde{H}_0 + \hat{T}_y + \hat{V}_{\text{conf}} + \hat{U}_{\text{int}} + \frac{\delta}{2} \sum_{m,n} [(-1)^m + (-1)^n] \hat{n}_{m,n},$$

$$\text{(S.15)}$$

which signals the absence of tunneling along the x direction at the lowest order of the calculations.

The first-order terms

The first-order contributions to the effective Hamiltonian are given by

$$\hat{H}_{\text{eff}}^{(1)} = \frac{1}{\hbar\omega}[\hat{V}^{(+1)}, \hat{V}^{(-1)}] = J_x^{\text{eff}} \sum_{m,n} \hat{a}_{m+1,n}^{\dagger} \hat{a}_{m,n} e^{i\phi_{m,n}} + \text{h.c.},$$

$$J_x^{\text{eff}} = J_x \frac{\kappa}{\sqrt{2}\hbar\omega}, \quad \phi_{m,n} = [\pi/2(m+n) - \phi_0], \quad (\text{S.16})$$

hence simultaneously restoring the hopping along the x direction and generating space-dependent Peierls phases $\phi_{m,n}$. In the experiment, the parameters are chosen such that the hopping is approximately homogeneous along both spatial directions, yielding $J_x^{\text{eff}} \approx J_y \approx 75\text{Hz} \times h$. Consequently, the first-order contributions are as important as the zero-th order terms.

In summary, the first-order effective Hamiltonian reproduces the Harper-Hofstadter model [S4] with a uniform flux $\Phi = 2\pi(1/4) = \pi/2$ per plaquette,

$$\hat{H}_{\text{eff}} = \hat{H}_{\text{eff}}^{(0)} + \hat{H}_{\text{eff}}^{(1)}, \quad (\text{S.17})$$

$$= J_x^{\text{eff}} \sum_{m,n} \left\{ \hat{a}_{m+1,n}^{\dagger} \hat{a}_{m,n} e^{i[\pi/2(m+n)-\phi_0]} + \text{h.c.} \right\}$$

$$- J_y \sum_{m,n} \left\{ \hat{a}_{m,n+1}^{\dagger} \hat{a}_{m,n} + \hat{a}_{m,n-1}^{\dagger} \hat{a}_{m,n} \right\} + \hat{V}_{\text{extra}},$$

$$\hat{V}_{\text{extra}} = \frac{\delta}{2} \sum_{m,n} [(-1)^m + (-1)^n] \hat{n}_{m,n} + \hat{V}_{\text{conf}} + \hat{U}_{\text{int}}.$$

At this order of the calculations, all additional effects [i.e. the static staggered potential detuning, the confinement and interactions] are assembled in $\hat{V}_{\text{extra}}$. Note that for the Hamiltonian given in eq. (1) of the main text and the discussion of the energy spectrum in Sect. S.IV of the Supplementary Information, we have chosen to describe our system in the Landau gauge $\phi_{m,n} = n\pi/2$ for the sake of simplicity.

The second-order terms

The second-order contributions lead to four distinct corrections:

$$\hat{H}_{\text{eff}}^{(2)} = \frac{1}{2(\hbar\omega)^2} \left([[\hat{V}^{(+1)}, \tilde{H}_0], \hat{V}^{(-1)}] + [[\hat{V}^{(-1)}, \tilde{H}_0], \hat{V}^{(+1)}] \right)$$

$$= \mathcal{C}_1 + \mathcal{C}_2 + \mathcal{C}_3 + \mathcal{C}_4.$$

In the following, we omit the high-order contributions stemming from the on-site interaction term $\hat{U}_{\text{int}}$, which lead to negligible delocalized interaction terms.

The first and main correction is a space-dependent renormalization of the hopping along the y direction:

$$\mathcal{C}_1 = -J_y \left(\frac{\kappa}{2\hbar\omega}\right)^2 \sum_{m,n} \mu_{m,n} \hat{a}_{m,n+1}^{\dagger} \hat{a}_{m,n} + \text{h.c.}$$

$$\mu_{m,n} = -2 + 2(-1)^{m+n} \cos(2\phi_0). \quad (\text{S.18})$$

Thus, taking into account this second-order correction, we find that the hopping amplitude is potentially inhomogeneous

along the y direction, and that it ranges between $J_y^{\text{eff}} = J_y$ and $J_y^{\text{eff}} = J_y[1 - (\kappa/(\hbar\omega))^2]$. As discussed in the next Section, the parameter $\kappa/(\hbar\omega) \approx 0.58$ in the experiment, so that this effect cannot be safely neglected.

The three other corrections are very weak, and thus, they can be neglected in the regimes explored by the experiment. To be explicit, the second correction is a weak next-nearest-neighbor hopping term of the form

$$\mathcal{C}_2 = \frac{\kappa J_x J_y}{(\hbar\omega)^2} \sum_{m,n} e^{i\theta_1} \hat{a}_{m+1,n+1}^{\dagger} \hat{a}_{m,n} + e^{i\theta_2} \hat{a}_{m-1,n+1}^{\dagger} \hat{a}_{m,n}$$

$$+ e^{i\theta_3} \hat{a}_{m+1,n-1}^{\dagger} \hat{a}_{m,n} + e^{i\theta_4} \hat{a}_{m-1,n-1}^{\dagger} \hat{a}_{m,n}.$$

The third effect is an even weaker correction to the nearest-neighbor hopping term along x,

$$\mathcal{C}_3 = \frac{\kappa J_x}{2(\hbar\omega)^2} \sum_{m \text{ odd},n} \lambda_{m,n} \hat{a}_{m+1,n}^{\dagger} \hat{a}_{m,n} + \tilde{\lambda}_{m,n} \hat{a}_{m-1,n}^{\dagger} \hat{a}_{m,n} + \text{h.c.}$$

where $\lambda_{m,n}$ and $\tilde{\lambda}_{m,n}$ depend linearly on the additional (weak) potentials in $\hat{V}_{\text{extra}}$, see eq. (S.17). The fourth effect $\mathcal{C}_4$ is a negligible next-nearest-neighbor hopping term proportional to $J_x J_y/(\hbar\omega)^2 \ll 1$.

Summary

In conclusion, in the parameters regime considered in the experiment, we find that the dynamics should be well described by the first-order effective (Harper-Hofstadter) Hamiltonian in eq. (S.17), including the second-order corrections $\mathcal{C}_1$ presented in eq. (S.18):

$$\hat{H}_{\text{eff}} = -J \sum_{m,n} \left\{ \hat{a}_{m+1,n}^{\dagger} \hat{a}_{m,n} e^{i[\pi/2(m+n)-\phi_0]} + \text{h.c.} \right.$$

$$\left. + (1 + f_{m,n}) \hat{a}_{m,n+1}^{\dagger} \hat{a}_{m,n} + \text{h.c.} \right\}$$

$$+ \frac{\delta}{2} \sum_{m,n} [(-1)^m + (-1)^n] \hat{n}_{m,n} + \hat{V}_{\text{conf}} + \hat{U}_{\text{int}}, \quad (\text{S.19})$$

where we introduced the correction to the hopping along y

$$f_{m,n} = -\frac{1}{2} \left(\frac{\kappa}{\hbar\omega}\right)^2 \left\{ 1 - (-1)^{m+n} \cos(2\phi_0) \right\}, \quad (\text{S.20})$$

and where we set $J = J_y$. Moreover, in this regime the static linear gradient used to generate the Hall drift can be simply added according to

$$\hat{H}_{\text{eff}} \rightarrow \hat{H}_{\text{eff}} - Fa \sum_{m,n} n \hat{n}_{m,n}.$$

S.IV. ENERGY SPECTRUM AND MAGNETIC UNIT CELL

The energy spectrum of non-interacting particles in a periodic potential exposed to an external magnetic field is described by the well-known Hofstadter butterfly [S4]. This

structure can be understood, starting from a simple tight-binding description. In the absence of the magnetic field, the tight-binding approximation leads to a single energy band, $E = -2J[\cos(k_x a) + \cos(k_y a)]$, where J is the tunneling matrix element between neighboring sites. Adding the magnetic field, through the introduction of Peierls phases [S4], leads to a fractionalization of the tight-binding band into several subbands: in particular, when the magnetic flux per plaquette is given by $\Phi = 2\pi\alpha = 2\pi(p/q)$, with p, q integers, the band splits into q subbands. In our experimental setup $\alpha = 1/4$, so that the energy spectrum is constituted of four subbands. Besides, the magnetic flux effectively extends the standard unit cell of the lattice into a "magnetic unit cell", which in this case is constituted of $q = 4$ lattice sites. In the following, and for the sake of simplicity, we have chosen to describe the system using the Landau gauge together with a square ["symmetric"] 4-site unit cell, see the gray shaded area in Fig. 1a of the main text and below.

We start with the Schrödinger equation associated with the Harper-Hofstadter model [S4],

$$\varepsilon\Psi_{m,n} = e^{in\pi/2}\Psi_{m+1,n} + e^{-in\pi/2}\Psi_{m-1,n} + \Psi_{m,n+1} + \Psi_{m,n-1},$$

which describes hopping on the square lattice in the presence of a magnetic flux $\Phi = \pi/2$ per plaquette. Here $\varepsilon = -E/J$, (m, n) are integers labeling the lattice sites, and for now, we considered that the hopping is homogeneous along both directions (i.e. $J_x^{\text{eff}} = J_y = J$ in terms of the experimental parameters discussed in the previous section). To solve this equation, we make the following ansatz for the wave function:

$$\Psi_{m,n} = e^{ik_x m} e^{ik_y n} \begin{cases} \psi_A, & \text{for } m, n \text{ even} \\ \psi_B\, e^{in\pi/2} & \text{for } m \text{ odd}, n \text{ even} \\ \psi_C & \text{for } m \text{ even}, n \text{ odd} \\ \psi_D\, e^{in\pi/2} & \text{for } m, n \text{ odd} \end{cases}$$

where k_x, k_y are defined within the first magnetic Brillouin zone ($k_x \in [-\pi/(2a), \pi/(2a)[$, $k_y \in [-\pi/(2a), \pi/(2a)[$). Inserting this ansatz into the Schrödinger equation we obtain the following 4×4 eigenvalue equation

$$\hat{H} \begin{pmatrix} \psi_A \\ \psi_B \\ \psi_C \\ \psi_D \end{pmatrix} = E(\mathbf{k}) \begin{pmatrix} \psi_A \\ \psi_B \\ \psi_C \\ \psi_D \end{pmatrix}, \tag{S.21}$$

with

$$\hat{H} = -2J \begin{pmatrix} 0 & \cos k_x & \cos k_y & 0 \\ \cos k_x & 0 & 0 & -\sin k_y \\ \cos k_y & 0 & 0 & -i\sin k_x \\ 0 & -\sin k_y & i\sin k_x & 0 \end{pmatrix}, \tag{S.22}$$

where we set $a = 1$.

Adding the staggered potential detuning (see main text and eq. (S.17) above),

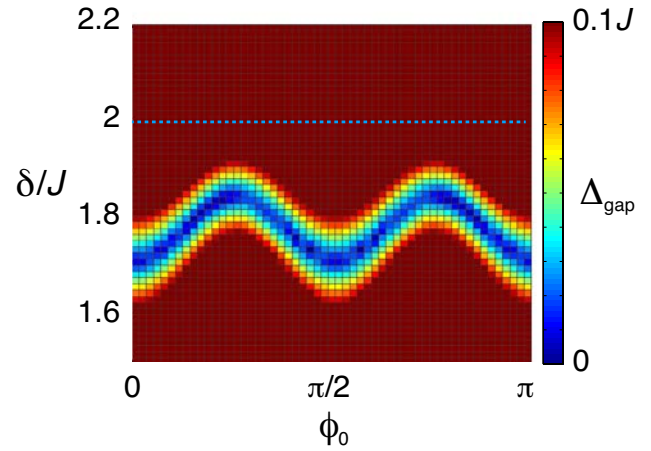$$\frac{\delta}{2} \sum_{m,n} [(-1)^m + (-1)^n]\, \hat{n}_{m,n},$$

FIG. S3. Gap closing point, separating the topological and non-topological regimes, as a function of the staggered potential detuning δ and the relative phase ϕ_0 for $\kappa/(\hbar\omega) = 0.58$. Here $J_x^{\text{eff}} = J_y = J$, where J_y is the bare tunneling amplitude along y. The blue dotted line shows the transition point for the homogeneous Harper-Hofstadter model in eq. (S.23), i.e. $J_x^{\text{eff}} = J_y^{\text{eff}} = J$.

where $\hat{n}_{m,n}$ is the particle number operator at lattice site (m, n), leads to the modified Hamiltonian matrix

$$\hat{H} \to \hat{H} = -2J \begin{pmatrix} (-\delta/2J) & \cos k_x & \cos k_y & 0 \\ \cos k_x & 0 & 0 & -\sin k_y \\ \cos k_y & 0 & 0 & -i\sin k_x \\ 0 & -\sin k_y & i\sin k_x & (\delta/2J) \end{pmatrix}. \tag{S.23}$$

Finally, to build the complete effective Hamiltonian, we consider the contribution of the inhomogeneous hopping along the y direction, which stems from the second-order corrections in eq. (S.18), see Section S.III. The total hopping term along the y direction [including the zero-th order "bare" hopping and the second-order corrections] is written as [eq. (S.19)]

$$\hat{T}_y = -J \sum_{m,n} (1 + f_{m,n})\hat{a}_{m,n+1}^\dagger \hat{a}_{m,n}$$
$$+ (1 + f_{m,n-1})\hat{a}_{m,n-1}^\dagger \hat{a}_{m,n},$$
$$f_{m,n} = -\frac{1}{2}\left(\frac{\kappa}{\hbar\omega}\right)^2 \left\{1 - (-1)^{m+n}\cos(2\phi_0)\right\}, \tag{S.24}$$

where we set $J = J_y$ is the bare hopping along the y direction (and we remind that $J_x^{\text{eff}} = J_y = J$). Taking these corrections into account (see Section S.III) leads to the final effective Hamiltonian matrix as given in the Method section of the main text

$$\hat{H}_{\text{eff}} = -2J \begin{pmatrix} (-\delta/2J) & \cos k_x & \cos k_y + h_1 & 0 \\ \cos k_x & 0 & 0 & -\sin k_y + h_2^* \\ \cos k_y + h_1^* & 0 & 0 & -i\sin k_x \\ 0 & -\sin k_y + h_2 & i\sin k_x & (\delta/2J) \end{pmatrix}$$

$$h_1 = -\frac{1}{2}\left(\frac{\kappa}{\hbar\omega}\right)^2 [\cos k_y - i\cos(2\phi_0)\sin k_y]$$

$$h_2 = \frac{1}{2}\left(\frac{\kappa}{\hbar\omega}\right)^2 [\sin k_y + i\cos(2\phi_0)\cos k_y]. \tag{S.25}$$

In the experiment, $\kappa/(\hbar\omega) \approx 0.58$, so that the effects related to the inhomogeneous hopping along the y direction cannot

be neglected [i.e. the hopping can potentially be reduced locally by 30%]. We illustrate this effect by computing the gap closing point, separating the topological and non-topological regimes and driven by the staggered potential detuning δ, for $\kappa/(\hbar\omega) = 0.58$ and $\phi_0 \in [0,\pi]$. As shown in Fig. S3, the ideal transition point $\delta = 2J$, corresponding to the homogeneous Harper-Hofstadter model (S.23) [$J_x^{\text{eff}} = J_y^{\text{eff}}$], is shifted and oscillates as a function of the relative phase ϕ_0. We find that these effects are of the order of experimental uncertainties, indicating that higher-order effects can be safely neglected in the analysis. In particular, omitting the effects due to the external trap and inter-particle interactions, we find that the setup and its phase transitions are well described by the 4×4 Hamiltonian matrix in eq. (S.25).

S.V. THE ANOMALOUS VELOCITY, THE HALL DRIFT AND THE EFFECTIVE CHERN NUMBER

General discussion

We start the discussion by considering a square lattice subjected to a general flux per plaquette $\alpha = p/q$ [in units of the flux quantum, i.e. $\Phi = 2\pi\alpha$]. Each "magnetic" unit cell of the lattice contains q lattice sites, and the energy spectrum splits into q subbands. In the case where these bands are well separated, the number of states available in each subband is $N_{\text{state}} = N_x N_y$, where $N_{x,y}$ are the numbers of magnetic unit cells along each spatial direction [there are then $qN_x N_y$ lattice sites in the system].

The q bands are labelled as $\varepsilon_\mu(k_x, k_y)$, where $\mu = 1, \ldots, q$, and the quasi-momenta [Bloch parameters] take the values

$$k_x = \frac{2\pi n_x}{L_x}, \quad k_y = \frac{2\pi n_y}{L_y}, \quad n_{x,y} = 1, \ldots, N_{x,y}, \quad \text{(S.26)}$$

$$\Delta_{k_x} = \frac{2\pi}{qN_x a}, \quad \Delta_{k_y} = \frac{2\pi}{N_y a}, \quad \text{(S.27)}$$

where we have chosen the magnetic unit cell to have length qa along the x direction, such that the overall system has lengths $L_x = qN_x a$ and $L_y = N_y a$ (In the main text, for $q = 4$, the magnetic unit cell is chosen to have size $2a \times 2a$, such that $L_{x,y} = 2N_{x,y}a$ and the resulting magnetic Brillouin zone is symmetric with respect to k_x and k_y. The first "magnetic" Brillouin zone (FBZ) is defined by

$$k_x \in (-\pi/qa, \pi/qa], \quad k_y \in (-\pi/a, \pi/a]. \quad \text{(S.28)}$$

We act on the particles with a force $\boldsymbol{F} = F\hat{\mathbf{e}}_y$, aligned along y, and we focus the following analysis on the velocity $v = v^x$ defined in the direction perpendicular to the force. The average velocity in a state $|u_\mu(k_x, k_y)\rangle$ associated with the energy $\varepsilon_\mu(k_x, k_y)$ is given by [S5]

$$v_\mu(k_x, k_y) = v_\mu^{\text{band}} - \frac{F}{\hbar}\Omega_\mu(\boldsymbol{k}), \quad \text{(S.29)}$$

where $\Omega_\mu(\boldsymbol{k})$ is the Berry curvature of the μ-th band,

$$\Omega_\mu(\boldsymbol{k}) = i\left(\langle\partial_{k_x} u_\mu|\partial_{k_y} u_\mu\rangle - \langle\partial_{k_y} u_\mu|\partial_{k_x} u_\mu\rangle\right), \quad \text{(S.30)}$$

and $v_\mu^{\text{band}} = (1/\hbar)\partial_{k_x}\varepsilon_\mu$ is the standard band velocity along x. The contribution due to the Berry's curvature in eq. (S.29) is generally referred to as the "anomalous velocity", see Ref. [S5].

We now populate each band ε_μ with $N^{(\mu)}$ particles. We assume that these particles uniformly distribute themselves over the entire band (this assumption is validated experimentally through the band-mapping technique, see also Sect. S.VI). We write the total number of particles as

$$N_{\text{tot}} = N^{(1)} + N^{(2)} + \cdots + N^{(\mu)} + \cdots + N^{(q)}. \quad \text{(S.31)}$$

The mean number of particles in a state $|u_\mu(k_x, k_y)\rangle$ is then given by

$$\rho^{(\mu)}(\boldsymbol{k}) = \frac{N^{(\mu)}}{N_x N_y} = \rho^{(\mu)}. \quad \text{(S.32)}$$

The mean velocity per particle is given by

$$\begin{aligned}\langle v\rangle &= \frac{1}{N_{\text{tot}}}\sum_\mu\sum_{\boldsymbol{k}}\rho^{(\mu)}(\boldsymbol{k})\,v^{(\mu)}(\boldsymbol{k}), \\ &= \frac{1}{N_{\text{tot}}}\sum_\mu\rho^{(\mu)}\sum_{\boldsymbol{k}}\left(-\frac{F}{\hbar}\Omega_\mu(\boldsymbol{k})\right), \\ &= \frac{1}{N_{\text{tot}}}\sum_\mu\rho^{(\mu)}\left(-\frac{2\pi}{\hbar}F\Delta_{k_x}^{-1}\Delta_{k_y}^{-1}\right)\underbrace{\frac{1}{2\pi}\sum_{\boldsymbol{k}}\Omega_\mu(\boldsymbol{k})\Delta_{k_x}\Delta_{k_y}}_{\to\nu_\mu}, \\ &= \frac{1}{N_{\text{tot}}}\sum_\mu\rho^{(\mu)}\left(-\frac{FqN_x N_y a^2}{h}\right)\nu_\mu, \\ &= \frac{1}{N_{\text{tot}}}\sum_\mu N^{(\mu)}\left(-\frac{Fqa^2}{h}\right)\nu_\mu,\end{aligned}$$

where we introduced the Chern number ν_μ of the μ-th band [S6, S7, S8]

$$\nu_\mu = \frac{1}{2\pi}\int_{\text{FBZ}}\Omega_\mu(\boldsymbol{k})\mathrm{d}^2 k. \quad \text{(S.33)}$$

Here, the velocity has no contribution from the band velocity $\partial_{k_x}\varepsilon_\mu$, which vanishes by symmetry when the band is uniformly filled [S5, S9, S11].

Introducing the band filling factor η_μ, we finally find the mean velocity per particle

$$\langle v\rangle = -\frac{Fqa^2}{h}\sum_\mu\eta_\mu\nu_\mu, \quad \eta_\mu = N^{(\mu)}/N_{\text{tot}}.$$

For $\eta_\mu(t) = \eta_\mu^0$ constant in time, the center-of-mass displacement along the x direction is thus given by

$$x(t) = x(t_0) - \frac{Ftqa^2}{2\pi\hbar}\sum_\mu\eta_\mu^0\nu_\mu. \quad \text{(S.34)}$$

We stress that we assumed that the force F is weak enough so that the band populations remain constant during the motion.

If only the lowest band is filled, i.e. $\eta_1^0 = 1$ and $\eta_{\mu>1}^0 = 0$, we find

$$x(t) = x(t_0) - \frac{Ftqa^2}{2\pi\hbar}\nu_1, \quad \text{(S.35)}$$

where ν_1 is the Chern number of the filled (lowest) band [S11].

Energy spectrum displaying band touching points: the case $\Phi = 1/4$

When the flux is $\Phi = \pi/2$ [i.e. $\alpha = 1/4$ and $q = 4$], as it is the case in the experiment [see eq. (S.17)], the energy spectrum only displays *three well separated bands* (see Fig. S4a and Fig.2 in the main text). The central "super-band" consists of two touching subbands [S8]: ε_2 and ε_3. Since the Chern number is only well defined for isolated bands [S6, S8], it is important to consider the new following labeling of bands:

$$E_1 = \varepsilon_1, \quad E_2 = "\varepsilon_2 + \varepsilon_3", E_3 = \varepsilon_4. \quad (S.36)$$

The Chern numbers $\nu_{1,2,3}$ associated with these well-separated bands have the values $\{1, -2, 1\}$, see Ref. [S8].

We now fill each band E_μ with $N^{(\mu)}$ particles, and $\mu = 1, 2, 3$. As before, we assume that these particles uniformly distribute themselves over each band. We write the total number of particles as

$$N_{\text{tot}} = N^{(1)} + N^{(2)} + N^{(3)}. \quad (S.37)$$

The mean number of particles in a state of the lowest or upper bands are

$$\rho^{(1)} = \frac{N^{(1)}}{N_x N_y}, \quad \rho^{(3)} = \frac{N^{(3)}}{N_x N_y}, \quad (S.38)$$

whereas in the central band, the mean number of particles is

$$\rho^{(2)} = \frac{N^{(2)}}{2N_x N_y}, \quad (S.39)$$

since the second "super-band" contains $2N_x N_y$ states. The mean velocity per particle is then obtained as in the previous Section,

$$
\begin{aligned}
\langle v \rangle &= \frac{1}{N_{\text{tot}}} \sum_{\mu=1,2,3} \rho^{(\mu)} \sum_{\boldsymbol{k}} \left(-\frac{F}{\hbar} \Omega_\mu(\boldsymbol{k}) \right), \\
&= -\frac{F}{\hbar N_{\text{tot}}} \left[\rho^{(1)} \sum_{\boldsymbol{k}} \Omega_1(\boldsymbol{k}) + \rho^{(2)} \sum_{\boldsymbol{k}} \Omega_2(\boldsymbol{k}) + \rho^{(3)} \sum_{\boldsymbol{k}} \Omega_3(\boldsymbol{k}) \right], \\
&= -\frac{4Fa^2}{h N_{\text{tot}}} \left[N^{(1)} \nu_1 + \frac{N^{(2)}}{2} \nu_2 + N^{(3)} \nu_3 \right], \\
&= -\frac{4Fa^2}{h} \left[\eta_1 \nu_1 + \frac{\eta_2}{2} \nu_2 + \eta_3 \nu_3 \right],
\end{aligned}
$$

where we again introduced the band filling factor $\eta_\mu = N^{(\mu)}/N_{\text{tot}}$, and the Chern numbers ν_μ of the three separated bands, $\mu = 1, 2, 3$. Accordingly, for $\eta_\mu(t) = \eta_\mu^0$ constant in time, the center-of-mass displacement is given by

$$x(t) = x(t_0) - \frac{2Fta^2}{\pi\hbar} \left[\eta_1^0 \nu_1 + \frac{\eta_2^0}{2} \nu_2 + \eta_3^0 \nu_3 \right], \quad (S.40)$$

so that measuring the initial fillings $\eta_{1,2,3}^0$ give access to the Chern number ν_1, using symmetry arguments. Indeed, in the next paragraph we show that $\nu_1 = \nu_3$, which is a direct consequence of the particle-hole symmetry inherent to the Harper-Hofstadter model [S4, S8]. Using this symmetry, together with
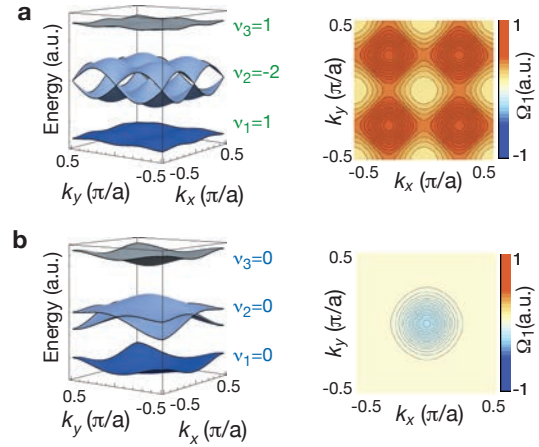
FIG. S4. Energy spectrum, Chern number distribution and Berry curvature of the lowest band for the Harper-Hofstadter Hamiltonian with flux $\Phi = \pi/2$. **a** the topological case $\delta = 0$, and **b** the topologically trivial case triggered by the staggered potential detuning, here illustrated for $\delta = 4J$. In contrast to the topologically trivial case, the Berry curvature has only positive contributions in the topological regime, leading to a non-zero Chern number $\nu_1 = +1$.

the fact that the total tight-binding band carries a zero Chern number, i.e. $\sum_j \nu_j = 0$, yields

$$\nu_2 = -2\nu_1, \quad \nu_3 = \nu_1, \quad (S.41)$$

so that eq. (S.40) becomes

$$x(t) = x(t_0) - \frac{2Fta^2}{\pi\hbar} \nu_1 \left[\eta_1^0 - \eta_2^0 + \eta_3^0 \right]. \quad (S.42)$$

We can rewrite the latter result as

$$x(t) = x(t_0) - \frac{2Fta^2}{\pi\hbar} \nu_1^{\text{eff}} \quad (S.43)$$

$$\nu_1^{\text{eff}} = \nu_1 \gamma_0, \quad \gamma_0 = \left[\eta_1^0 - \eta_2^0 + \eta_3^0 \right], \quad (S.44)$$

where ν_1^{eff} denotes the effective Chern number, which deviates from the ideal and quantized value ν_1 when higher bands are initially populated [i.e. $\eta_1^0 < 1$].

When the populations vary in time, as it is the case in the experiment, the center-of-mass follows the equations of motion

$$x(t) = x(t_0) - \frac{2Fa^2}{\pi\hbar} \nu_1 \int_0^t \eta_1(t') - \eta_2(t') + \eta_3(t') \mathrm{d}t'. \quad (S.45)$$

Hence, measuring the populations $\gamma(t) = \eta_1(t) - \eta_2(t) + \eta_3(t)$ together with the COM displacement $x(t)$ allows to evaluate the Chern number ν_1, based on long-time dynamics.

Finally, we note that an alternative analysis can be performed without invoking the particle-hole symmetry leading to eqs. (S.41)-(S.42). Indeed, by imposing $\sum_j \nu_j = 0$ only, the Hall deflection $x(t)$ can be fitted using the more general equation

$$
\begin{aligned}
x(t) = x(t_0) - \frac{2Fa^2}{\pi\hbar} \Bigg(& \nu_1 \int_0^t \eta_1(t') - \eta_3(t') \mathrm{d}t' \\
& + \nu_2 \int_0^t \frac{\eta_2(t')}{2} - \eta_3(t') \mathrm{d}t' \Bigg),
\end{aligned}
\quad (S.46)
$$

where the two fitting parameters are the Chern numbers of the two lowest bands $\nu_{1,2}$. We verified that this leads to a simultaneous and satisfactory measurement of these two topological numbers: For the data shown in Fig.3b of the main text we obtain $\nu_1 = 1.21(14)$, $\nu_2 = -2.7(5)$ (black data points) and $\nu_1 = 1.04(10)$, $\nu_2 = -2.2(3)$ (gray data points), where we have used the measured band populations $\eta_\mu(t)$ in Fig. 3c of the main text.

In Figure S4 we show the energy spectrum and the Berry curvature distribution of the lowest band for the homogeneous Harper-Hofstadter Hamiltonian ($\delta = 0$) in eq. (S.23). In the experiment, the additional staggered detuning δ triggers a topological phase transition at $\delta = 2J$ (Fig.4b in the main text and Sect. S.IV). For $\delta > 2J$, the bands are all topologically trivial, with Chern numbers $\nu_\mu = 0$, as depicted in Fig. S4b for $\delta = 4J$.

On the particle-hole symmetry and the Chern numbers

The discrete Schrödinger equation associated with the Harper-Hofstadter model can be written in the form [S4, S8]

$$E\psi(m,n) = -J\big[\psi(m+1,n) + \psi(m-1,n)$$
$$+ e^{i2\pi\alpha m}\psi(m,n+1) + e^{-i2\pi\alpha m}\psi(m,n-1)\big], \quad (S.47)$$

where we explicitly used the Landau gauge $\boldsymbol{B} = B(0,x)$, and we stress that the following discussion does not depend on this choice. For $\alpha = p/q$, the system has a discrete translational invariance associated with the translation operators

$$\hat{T}_x^q\psi(m,n) = \psi(m+q,n), \quad \hat{T}_y\psi(m,n) = \psi(m,n+1).$$

Using Bloch's theorem, we write the wave function as

$$\psi(m,n) = e^{ik_x m}e^{ik_y n}u_{\boldsymbol{k}}(m), \quad u_{\boldsymbol{k}}(m+q) = u_{\boldsymbol{k}}(m),$$

where the periodic function $u_{\boldsymbol{k}}(m)$ satisfies the equation

$$Eu_{\boldsymbol{k}}(m) = -J\big[u_{\boldsymbol{k}}(m+1)e^{ik_x} + u_{\boldsymbol{k}}(m-1)e^{-ik_x}$$
$$+ 2\cos(2\pi\alpha m + k_y)\,u_{\boldsymbol{k}}(m)\big]. \quad (S.48)$$

The energy spectrum splits into several subbands $E_\mu(\boldsymbol{k})$, where μ is the band index. Let us focus on a specific band $E_\mu(\boldsymbol{k})$, located around the value $E^* < 0$. The Chern number associated with this band is given by eq. (S.33), namely,

$$\nu_\mu = \frac{1}{2\pi}\int_{\text{FBZ}} \Omega_\mu(\boldsymbol{k})\mathrm{d}^2k. \quad (S.49)$$

Now, let us show that the Chern number associated with the "top band" $E_{\tilde{\mu}}(\boldsymbol{k})$, located around the value $(-E^*) > 0$ is the same as the Chern number of the "bottom band" $E_\mu(\boldsymbol{k})$, considered above: $\nu_\mu = \nu_{\tilde{\mu}}$. We start with the Harper equation (S.47) and consider the transformation

$$\psi(m,n) \rightarrow \tilde{\psi}(m,n) = (-1)^{m+n}\psi(m,n). \quad (S.50)$$

The new functions satisfy the Harper equation,

$$(-E)\tilde{\psi}(m,n) = -J\big[\tilde{\psi}(m+1,n) + \tilde{\psi}(m-1,n)$$
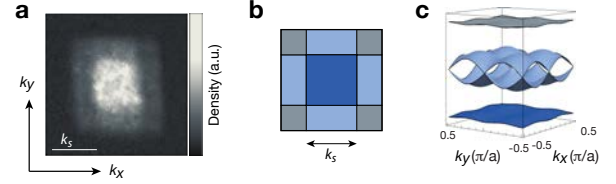$$+ e^{i2\pi\alpha m}\tilde{\psi}(m,n+1) + e^{-i2\pi\alpha m}\tilde{\psi}(m,n-1)\big], \quad (S.51)$$

FIG. S5. Momentum distribution of the atoms in the three well-separated Hofstadter bands. **a** This data was obtained after applying the loading and band-mapping sequence as described in the Method section of the main text. Here we show an average of 15 independent measurements obtained after 10 ms time-of-flight. **b** Schematic illustration of the corresponding Brillouin zones. **c** Energy spectrum of the Harper-Hofstadter model for $\Phi = \pi/2$. The color code illustrates the connection between the Brillouin zones and the Hofstadter bands.

which is the same as in eq. (S.47), but with $E \rightarrow -E$. This latter result illustrates the particle-hole symmetry in the system, i.e., the fact that if there exists a state at E, then there necessarily exists a state at the opposite energy $-E$ [which can be traced back to the fact that the square lattice is bipartite]. As before, we write the solution of eq. (S.51) as

$$\tilde{\psi}(m,n) = e^{ik_x m}e^{ik_y n}\tilde{u}_{\boldsymbol{k}}(m), \quad \tilde{u}_{\boldsymbol{k}}(m+q) = \tilde{u}_{\boldsymbol{k}}(m),$$

where the periodic functions $\tilde{u}_{\boldsymbol{k}}(m)$ satisfy the equation

$$E\tilde{u}_{\boldsymbol{k}}(m) = -J\big[\tilde{u}_{\boldsymbol{k}}(m+1)e^{i(k_x+\pi)} + \tilde{u}_{\boldsymbol{k}}(m-1)e^{-i(k_x+\pi)}$$
$$+ 2\cos(2\pi\alpha m + (k_y+\pi))\,\tilde{u}_{\boldsymbol{k}}(m)\big]. \quad (S.52)$$

Comparing with eq. (S.48), we find that the eigenstates associated with the "top band" $E_{\tilde{\mu}}(\boldsymbol{k})$ [located around $(-E^*) > 0$] can be obtained from the eigenstates associated with the "bottom band" $E_\mu(\boldsymbol{k})$ [located around $E^* < 0$] through the relation

$$u_{k_x,k_y}(m) = \tilde{u}_{k_x+\pi,k_y+\pi}(m). \quad (S.53)$$

In other words, the "particle-hole" transformation in eq. (S.50), which transforms a state of energy E into a state of opposite energy $(-E)$, is also associated with the transformation $\boldsymbol{k} \rightarrow (k_x+\pi, k_y+\pi)$. Consequently, the Berry's curvatures associated with the two opposite bands are related by

$$\Omega_\mu(k_x,k_y) = \Omega_{\tilde{\mu}}(k_x+\pi, k_y+\pi), \quad (S.54)$$

namely, both bands share the same curvature, up to an overall shift in the Brillouin zone.

As a corollary, two opposite bands of the Harper-Hofstadter model [located around E^* and $(-E^*)$, respectively] necessarily share the same Chern number [see eq. (S.33)], as this quantity averages the Berry's curvature over the FBZ [i.e. the overall shift in eq. (S.54) can be eliminated by a redefinition of the FBZ].

S.VI. MOMENTUM DISTRIBUTION IN THE HOFSTADTER BANDS

The Hall drift as a response to an externally applied force given in eq. (3) of the main text is based on the assumption

that the distribution of bosonic atoms in the different Hofstadter bands is incoherent and homogeneous. To check this assumption independently in the experiment we mapped the band populations of the Hofstadter bands onto the ones of a static two-dimensional superlattice. This is achieved by reversing the loading sequence illustrated in Fig. 2 of the main text (see also Methods). After loading the atoms into the three well-separated Hofstadter bands, a staggered detuning δ is ramped up within 30 ms along both directions to suppress tunneling in the presence of the modulation (see main text and Methods). Switching off the modulation then maps the populations in the bands of the explicitly time-dependent Hamiltonian onto the ones of the static superlattice potential. The size of the Brillouin zone and thus the number of bands remains unchanged during the mapping sequence, such that the population of different k-states is preserved if scattering processes and heating effects during the ramp are neglected. Consequently the momentum distribution in the bands of the static superlattice potential reflects the one of the Hofstadter bands. All fields are then switched off adiabatically to map the quasimomentum distribution onto the real-space momentum distribution. After letting the atoms expand for 10 ms we measured the distribution using standard absorption imaging. The result is shown in Fig. S5a. The connection to the Brillouin zones and the bands of the Harper-Hofstadter Hamiltonian are illustrated by the schematic drawings in Fig. S5b,c. It can be seen that the atoms are distributed homogeneously over the lowest band. A fraction of atoms also populates the higher bands in a homogeneous manner. Our data is thus consistent with our assumption of homogeneous populations in the bands.

S.VII. BAND-POPULATION MEASUREMENT

The population in different Hofstadter bands can be measured using the sequence described in the previous section by counting the atoms in the different Brillouin zones. The zones are, however, connected which complicates the precise evaluation of the corresponding atom numbers. To simplify the counting we apply a slightly different sequence which allows us to transfer the atoms to higher Bloch bands such that they appear in well separated Brillouin zones. We first map the band populations of the Hofstadter bands onto the ones of the static two-dimensional lattice without periodic driving (see previous section). After having switched off the periodic modulation the staggered energy offset between neighboring sites is given by $\delta + \Delta$ along x and by δ along y. If these energy offsets are large enough compared to the bare couplings J_x and J_y, tunneling is suppressed and the populations in different Bloch bands correspond to populations on different sites N_q, $q = A, B, C, D$ (see Fig. S6). These can be measured by transferring the populations on different sites to higher Bloch bands and performing a subsequent band-mapping technique [S10]. The connection between the Hofstadter bands, sites in the unit cell and Brillouin zones is illustrated by the color code in Fig. S6. Using the measured site-populations N_q we evaluated the occupation in the three Hofstadter bands, $\eta_1 = N_A/N_{\rm tot}$, $\eta_2 = (N_B + N_C)/N_{\rm tot}$ and $\eta_3 = N_D/N_{\rm tot}$, where $N_{\rm tot}$ is the total atom number (Fig. S6e). By fitting an exponential to the corresponding filling factor $\gamma(t) = \eta_1(t) - \eta_2(t) + \eta_3(t)$ we
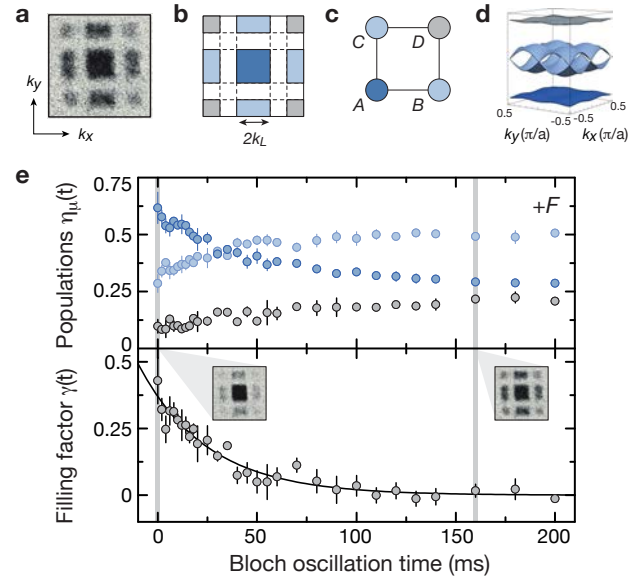

FIG. S6. Determination of the populations $\eta_\mu(t)$ and the corresponding filling factor $\gamma(t)$ in the three different Hofstadter bands. **a** Typical experimental image obtained after mapping the populations of the Hofstadter bands onto higher Bloch bands of the static two-dimensional superlattice as described in Sect. S.VII. The momentum distribution was measured after 10 ms time-of-flight. **b** Schematic drawing of the corresponding Brillouin zones. **c** Illustration of the four non-equivalent sites of the $2a \times 2a$ unit cell, whose dimensions are preserved during the sequence. **d** Energy spectrum of the Harper-Hofstadter model for $\Phi = \pi/2$. **e** Evolution of the band populations $\eta_\mu(t)$ as displayed in Fig. 3c of the main text and the corresponding filling factor $\gamma(t)$ for $Fa/h = 38.4(8)$Hz. The solid line in the lower panel shows an exponential fit to our data, which was used to extract the Chern number $\nu_{\rm exp}$. The color code illustrates the connection between the Brillouin zones, sites in the unit cell, the Hofstadter bands and the corresponding measured band populations $\eta_\mu(t)$. The insets in the lower panel show typical experimental images obtained after the band-mapping sequence.

determined the Chern number $\nu_{\rm exp}$ from the measured differential shift $2x(t)$ according to equation (5) in the main text, where ν_1 was the only free fit parameter.

S.VIII. ABSOLUTE CENTER-OF-MASS POSITIONS

To study the Hall deflection of the cloud we evaluated the differential shift for positive and negative flux Φ by subtracting the center-of-mass (COM) positions of the cloud as depicted in Fig. 3a,b of the main text. In this section we show the absolute COM positions of the cloud for positive (blue) and negative (red) sign of the flux corresponding to the black (Fig. S7a) and gray data points (Fig. S7b) in Fig. 3b of the main text. We observe a clear splitting of the positions perpendicular (x-direction) to the gradient for both directions $\pm F\hat{e}_y$. The additional drift in the x-position and differential shift in the y-position for $\mathbf{F} = F\hat{e}_y$ (Fig. S7a) is most likely due to a slight misalignment of the gradient such that it has a small component along x. We checked that this can be removed by aligning the optical gradient (see Method section of the main
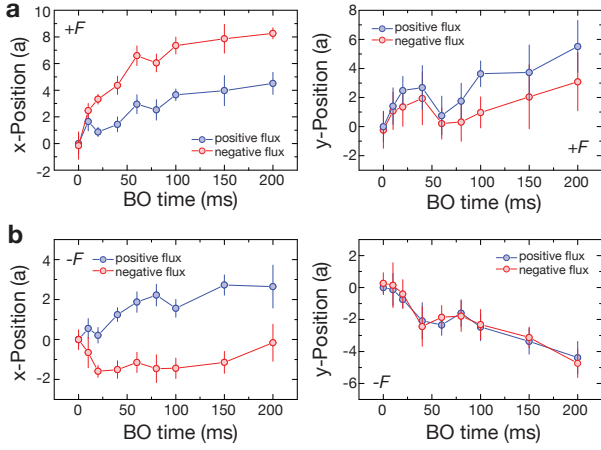
FIG. S7. Absolute center-of-mass positions along x and y as a function of the Bloch oscillation (BO) time for a gradient $\mathbf{F} = F\hat{\mathbf{e}}_y$ (a) and $\mathbf{F} = -F\hat{\mathbf{e}}_y$ (b) corresponding to the data shown in Fig. 3 of the main text.

text) more carefully as can be seen in Fig. S7b, where the data was taken just after aligning the optical gradient. The global drift along x in this case is absent as well as the differential shift along y. Additionally we checked that the differential shift perpendicular to the gradient is not affected.

S.IX. NUMERICAL SIMULATIONS AND SHORT-TIME DYNAMICS

In this Section, we discuss the methods used to simulate the dynamics. In the regime where the band populations $\eta_n(t) = \eta_n^0$ are constant, which is expected for sufficiently weak forces and short-time dynamics, the center-of-mass displacement follows the equations of motion,

$$x(t) = x(t_0) - \frac{2Fta^2}{\pi\hbar}\gamma_0\nu_1, \quad \gamma_0 = \eta_1^0 - \eta_2^0 + \eta_3^0, \quad \text{(S.55)}$$

as already discussed in Section S.V. For a given force F and initial band fillings η_n^0, this simple equation describes the "ideal" linear drift of the cloud.

In order to gain more insight on the dynamics captured by the effective Harper-Hofstadter Hamiltonian, and hence to verify the validity of eq. (S.55), we have simulated the full non-interacting problem. In the absence of the force F, we write the Hamiltonian ruling the dynamics as [eq. (S.19)]

$$\hat{H}_{\text{eff}} = -J\sum_{m,n}\{\hat{a}_{m+1,n}^{\dagger}\hat{a}_{m,n}e^{i[\pi/2(m+n)-\phi_0]} + \text{h.c.}$$
$$+ (1 + f_{m,n})\hat{a}_{m,n+1}^{\dagger}\hat{a}_{m,n} + \text{h.c.}\}$$
$$+ \frac{\delta}{2}\sum_{m,n}[(-1)^m + (-1)^n]\hat{n}_{m,n} + \hat{V}_{\text{conf}}, \quad \text{(S.56)}$$

which corresponds to the first-order effective Hamiltonian in eq. (S.17) together with the main second-order corrections $f_{m,n}$ defined in eq. (S.24). This Hamiltonian corresponds to the Harper-Hofstadter Hamiltonian with flux $\Phi = \pi/2$, and

it includes the staggered potential detuning, and the external harmonic potential $\hat{V}_{\text{conf}}$, see Section S.III. In the following, we take $\hat{V}_{\text{conf}} = \sum_{m,n} V(m,n)\hat{n}_{m,n}$, with the experimental configuration $V(m,n) = \beta(0.5m^2 + n^2)$ and $\beta = 10^{-3}J$. To simulate the dynamics in the presence of a force, we follow the strategy described in Ref. [S11]. We first establish the initial condition by confining the system within a certain radius $r_0 \sim 10 - 30a$, using a potential $\hat{V}_{\text{initial}}$; to simplify the analysis, we take an abrupt circular potential $\hat{V}_{\text{initial}} \sim (r/r_0)^{\zeta}$ with $\zeta \gg 10$, but we note that smoother potentials could also be considered for the initial preparation [S11]. We diagonalize the corresponding Hamiltonian matrix $\hat{H}_{\text{initial}} = \hat{H}_{\text{eff}} + \hat{V}_{\text{initial}}$ on a finite system of radius $r > r_0$, and we classify its eigenstates χ_α in terms of the three bulk bands, based on their energies E_α; we note that the three-band structure clearly appears in the density of states. Having established the initial population of the bands, we then compute the time evolution of each state $\chi_\alpha(t)$ according to the Hamiltonian $\hat{H}_{\text{evol}} = \hat{H}_{\text{eff}} + \hat{V}_{\text{force}}$, where $\hat{V}_{\text{force}} = -F\hat{y}$ describes the force acting on the particles at time $t > 0$ along the y direction; on the lattice, the operator $\hat{y}$ is defined as $\hat{y} = a\sum_{m,n} n\,\hat{n}_{m,n}$. The center-of-mass displacement $x(t)$ is then evaluated by computing the spatial density $\rho(\boldsymbol{x}, t)$, which is obtained from the populated evolving states $\chi_\alpha(t)$.
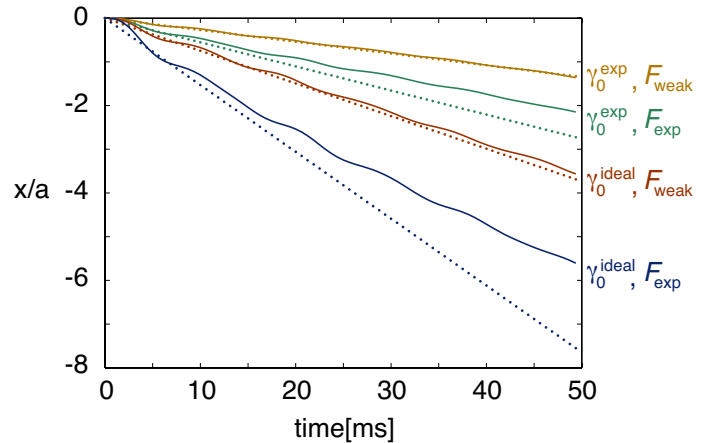

FIG. S8. Numerical simulations showing the center-of-mass displacement $x(t)$, in the direction perpendicular to the force $\boldsymbol{F} = F\hat{\mathbf{e}}_y$. The dynamics is governed by the Harper-Hofstadter Hamiltonian in eq. (S.56). The full curves correspond to different initial band populations and force strengths: the perfect filling of the lowest band is $\gamma_0^{\text{ideal}} = 1$, the experimental filling is $\gamma_0^{\text{exp}} = 0.36$, the "weak" force is $F_{\text{weak}} = 0.25J/a$ and the experimental force is $F_{\text{exp}} = 0.52J/a$. The dotted lines show the linear drift predicted by eq. (S.55) for each of the four situations; these linear trajectories are valid in the regimes where the band populations are constant (i.e. weak forces or short times). In all cases, we set $\delta = 0$, $\phi_0 = \pi/4$ and $\kappa/(\hbar\omega) = 0.58$, so that the effective tunneling along y is $J_y^{\text{eff}} \approx 0.83J$, and $J_x^{\text{eff}} = J$. As shown by the green shaded area in Fig. 3a of the main text, the trajectories are found to be similar for the wide range $\phi_0 \in [0, \pi]$.

Numerical results are illustrated in Fig. S8, where the center-of-mass displacement $x(t)$ is plotted for different initial band populations γ_0 and force strengths F. First, let us consider a

situation where the force is reasonably weak, $F_{\text{weak}} = 0.25 J/a$. In this case, the motion is found to follow the linear behavior predicted by (S.55), and the band populations remain approximatively constant for long times, $\gamma(t) = \gamma_0$. When the atoms populate the lowest band only, $\gamma_0^{\text{ideal}} = 1$, they all undergo a net drift along the $-x$ direction due to the positive Berry curvature associated with this band (see eq. (S.29) and Fig. S4). For a typical experimental filling $\gamma_0^{\text{exp}} = 0.36$, about 30% of the atoms populate the central band (with Chern number $\nu_2 = -2$), and they propagate in the opposite direction $+x$: this leads to a slower center-of-mass velocity, captured by the factor $\gamma_0 < 1$ in the equations of motion (S.55). Then, when the force is stronger, $F_{\text{exp}} = 0.52 J/a$, as it is the case in the experiment to optimize the displacement measurement, $\gamma(t)$ is no longer constant and the simulations show a clear deviation from the linear motion (S.55) for times $t \sim 20$ ms (both for $\gamma_0 = 1$ and $\gamma_0 < 1$). A comparison with our experimental data for times $t \leq 35$ ms is shown in Fig. 3a (main text), indicating a good agreement in the short-time regime. This short-time analysis, together with the measured initial band populations $\eta_\mu^0 = \{0.55(6), 0.31(3), 0.13(3)\}$, and the equations of motion in eq. (S.55), provides a reasonable experimental value for the Chern number of the lowest band $\nu_{\text{exp}} = 0.9(2)$. The green shaded area in Fig. 3a (main text) delimits the numerically simulated trajectories obtained in the range $\phi_0 \in [0, \pi]$, using the measured initial band populations ($\gamma_0 \approx 0.36$), and other experimental parameters ($\delta = 0$, $\kappa/(\hbar\omega) = 0.58$). As already illustrated in Fig. S8, the simulations already show a deviation from the linear behavior for times $t \sim 20$ ms; this explains the reduced value of the experimentally determined Chern number, which includes data points up to $t = 35$ ms. We point out that the linear-motion breakdown (i.e. the Landau-Zener induced inter-band transitions) signaled by our simulations only constitutes a partial explanation for the Hall drift saturation observed in the experiments. Indeed, we expect that additional effects, which are not captured by the present simulations (such as interactions and heating processes), could potentially lead to stronger band repopulation.

[S1] M. Aidelsburger, M. Atala, S. Nascimbène, S. Trotzky, Y.-A. Chen, and I. Bloch, Phys. Rev. Lett. **107**, 255301 (2011); M. Aidelsburger, M. Atala, S. Nascimbène, S. Trotzky, Y.-A. Chen, and I. Bloch, Appl. Phys. B **113**, 1 (2013).

[S2] N. Goldman and J. Dalibard, Phys. Rev. X **4**, 031027 (2014).

[S3] S. Rahav, I. Gilary, and S. Fishman, Phys. Rev. A **68**, 013820 (2003).

[S4] D. R. Hofstadter, Phys. Rev. B **14**, 2239 (1976).

[S5] D. Xiao, M. C. Chang and Q. Niu, Rev. Mod. Phys. **82**, 1959 (2010).

[S6] D. Thouless, M. Kohmoto, M. Nightingale, and M. den Nijs, Phys. Rev. Lett. **49**, 405 (1982).

[S7] B. Simon, Phys. Rev. Lett. **51**, 2167 (1983).

[S8] M. Kohmoto, Phys. Rev. B **39**, 11943 (1989).

[S9] H. M. Price and N. R. Cooper, Phys. Rev. A **85**, 033620 (2012).

[S10] S. Nascimbène *et al.*, Phys. Rev. Lett. **108**, 205301 (2012).

[S11] A. Dauphin and N. Goldman, Phys. Rev. Lett. **111**, 135302 (2013).